Evidence of twin mediated growth in the CVD of polycrystalline silicon carbide

Yann Gallou, Marie Dubois, Alexandre Potier, Didier Chaussende

Evidence of twin mediated growth in the CVD of polycrystalline silicon carbide

Yann Gallou[a,*], Marie Dubois[a], Alexandre Potier[b], Didier Chaussende[a]

[a] *Université Grenoble Alpes, CNRS, Grenoble INP (Institute of Engineering), SIMaP, 38000 Grenoble, FRANCE*

[b]*MERSEN, 41 rue Jean Jaurès, Gennevilliers, 92230, FRANCE*

Key words: Silicon carbide (SiC), Crystallographic orientation, EBSD, Twin boundary, Twin plane reentrant edge

ABSTRACT

The origin of the <110> texture in polycrystalline 3C-SiC grown by chemical vapor deposition at different temperatures is investigated by thorough EBSD, SEM and XRD characterizations. Regarding the <110> orientation, although XRD suggests a fiber texture, closer inspection of isolated clusters of grains by EBSD reveals a high symmetrical order in-plane. The pole figures associated with these clusters are in good agreement with cross-twinned pentagonal structures in which each grain shares a common <110> axis. These structures form via twin-mediated growth involving the formation of twin plane reentrant edges that act as a preferential site for the incorporation of adatoms. A deviation from a perfect cross-twinned structure is observed and is attributed to the presence of additional parallel twins. In this study, the transition to the <110> orientation occurs when the temperature increases and the partial pressure of reactive species decreases. This can be explained by the enhancement of surface mobility that promotes surface diffusion to the twin plane reentrant edges, thus activating the twin mediated growth mechanism.

I. Introduction

Due to its outstanding strength, hardness, and chemical and thermal shock resistance, polycrystalline silicon carbide (SiC) can be used for various applications requiring high temperatures, harsh environments and/or strong mechanical stresses. It can thus meet the needs of aerospace, nuclear engineering, defense applications, the chemical industry, and electronic and photonic applications. Chemical vapor deposition (CVD) can produce pure and dense SiC on different types of substrates. For instance, deposition on graphite can serve as a protective coating against oxidation or chemical reactions in semiconductor annealing and doping furnaces. Deposition on silicon can serve as a structure for fabricating MEMS which are used as resonators and sensors at high temperatures and in harsh conditions [1,2].

When deposited by CVD, a preferential orientation often forms with mainly <111> and <110> oriented samples being observed independently of the precursors used (SiH_4+C_3H_8; $SiCl_4$+C_3H_8, $SiCH_3Cl_3$) and the type of reactor (cold wall, hot wall, laser assisted) [3–12]. The mechanical properties, for example, of polycrystalline SiC films are affected by this preferential orientation. <111> oriented films exhibit both greater hardness [13–15] and a higher Young modulus [13,16] than <110> oriented ones. Grain size also plays a role [13–15]. Consequently, it is important to understand how this

preferential orientation occurs. From a theoretical viewpoint, studying preferential orientation and microstructure development can highlight the underlying growth mechanism. The selection of a preferential orientation in polycrystalline samples is commonly described by the Van der Drift mechanism, according to which orientation selection results from faster growth along specific crystallographic directions [17]. After a random nucleation process, the grains having their fastest orientation aligned with the normal to the surface will grow over the neighboring grains, leading to the formation of a preferential orientation. While this rule of evolutionary selection is widely accepted and has been demonstrated for polycrystalline SiC growth through cross-section analysis [8,11], the origin of the faster growth remains unclear.

Some authors have used surface energy to explain preferential growth on specific planes. Surface energy is correlated to ledge density due to the presence of additional dangling bonds at these specific sites. The number of ledges scales with the angle that the plane considered {hkl} forms with the close-packed plane, {111} in a face-centered cubic (FCC) lattice. Therefore, the surface energy increases in the order {111}, {100}, {110}, and is in general higher for higher {hkl} indexes [18,19]. It should be noted that adatoms are preferentially incorporated at ledges due to the higher number of bonds formed compared to terraces. In 1989, Lee [18,20] proposed a model in which the selection of a low or a high energy plane depends on the process conditions. Typically, at low temperature and low species concentration, the lower energy plane will grow preferentially to minimize the energy of the newly created surface. By combining a higher temperature, which enhances surface diffusion and a higher species concentration, which in turn increases the adsorption rate, the growth of higher energy planes is promoted due to the higher density of ledges. This simple model can roughly explain the transition from <111> to <110> orientation in polycrystalline 3C-SiC when the temperature increases, and has been invoked in some studies on texture transition in the CVD of polycrystalline SiC [6,9].

In 2002, Kajikawa et al. [7] proposed a mechanism based on two regimes: adsorption limited and surface reaction limited. This mechanism has been extensively invoked to account for texture transition in the CVD of polycrystalline SiC [9,21,22]. In their approach, they did not consider ledge density, instead, they used a Langmuir-type approach where each atom on a plane is an adsorption site for incoming species. In the surface reaction-limited regime, the incoming species flux is considered as unlimited, and the rate constant is independent of the planes considered. For the authors, this leads to faster growth of the most densely packed plane that is {111} in 3C-SiC, i.e. with the highest Si-C pair density. However, in this approach, the shorter d-spacing for the (111) planes (2.52 Angström) is not accounted whereas this would lead to slower normal growth compared to higher d-spacing planes, keeping the amount of incoming species constant. In the adsorption limited regime, the surface reaction rate exceeds that of the adsorption rate, hence the growth rate is limited by adsorption of new species, hence by the sticking coefficient of the plane considered. The authors claimed that {110} planes may have a higher sticking coefficient due to a higher atomic density (2.47×10^{-9} mol.cm^{-2}) and to the fact that these planes exhibit both Si and C atoms which enables the adsorption of either Si-species or C-species and the co-adsorption of species containing both Si and C atoms. They also claimed that the reactive species change from “monomer” to “polymer” when the residence time increases, having different sticking probabilities and in turn impacting the preferential orientation. However, these two

assumptions are not in accordance with the species originating from the thermal decomposition of the precursor, according to thermodynamic and kinetic modeling. Indeed, in standard chlorinated CVD, the main gas phase species are $SiCl_2$, $SiCl_3$, $SiCl_4$, $SiCl_3H$, SiCl, Si, SiH, CH_4, C_2H_2, C_2H_4, CH_3, and Si_2C over a broad range of temperature and the main intermediates for growth are supposed to be SiCl, SiH, Si, CH_3 and C_2H_2, independently of the precursor used [23–25]. Then for us, the reasons for a higher sticking coefficient on the {110} planes remain unclear.

Radmilovic et al [8] attributed the selection of the <111> orientation to the slow growth rate of the $\{\bar{1}\bar{1}\bar{1}\}$-C terminated planes compared to that of the {111}-Si terminated planes. This leads to the growth of a crystal with a tetrahedral shape bounded by triangular slow growing $\{\bar{1}\bar{1}\bar{1}\}$-C terminated planes and with a preferential direction along the <111> direction. The authors also suggested that the selection of the fastest <111> direction is assisted by twinning events. Twinning is likely to occur on the {111} planes due to the low stacking fault energy (1.5 $mJ.m^{-2}$) of 3C-SiC [26]. Starting from a grain having none of its fastest <111> directions aligned with the substrate's normal, each twinning event will lead to a change of the crystallographic direction normal to the substrate. After a succession of twinning, a <111> direction perpendicular to the substrate can finally be selected and further twinning will maintain it as it is.

Growth mechanisms based on twinning have also been proposed to account for the <110> texture in SiC [5,22,27–29]. However, only few authors have used TEM to analyze twins and micro-twins in SiC [11,28,30], and to our knowledge, no-one has fully characterized the twinned structure at the grain scale. Therefore, this paper is intended to fill this gap by describing a study comprising thorough electron back scatter diffraction (EBSD) analysis. We also discuss on the qualitative level the change of growth mechanism as a function of the local growth conditions and the resulting change of preferential orientation.

II. Experimental procedures

1. Sample fabrication

Samples were fabricated in a lab-scale vertical hot-wall CVD reactor. After sample loading and prior to deposition, argon was injected until atmospheric pressure was reached in the reactor and purged down to a pressure of 0.01 mbar. The operation was repeated three times. Then the reactor was let under vacuum with the pump on for at least 24 hours before deposition. This allows outgassing of the reactor after exposition to air during loading and unloading of the samples. The graphite chamber was heated via induction using a 55 kW generator, at 17 kHz. The heating phase was realized under hydrogen flow and lasted about an hour before thermal equilibrium was reached, prior to the injection of the precursor. The precursor was methyltrichlorosilane (MTS) diluted in H_2 using a ratio of 1:10. The inlet flow and pressure were set at 1050 sccm and several tens of mbar, respectively. The deposition lasted for an hour. After deposition, the power was gradually reduced during 15 minutes under H_2, allowing the reactor to cool down. Then H_2 flow was stopped and the reactor was put under vacuum (<0.01 mbar) and cooled down naturally down to ambient temperature. The samples were collected the next day.

The reactor has been designed to have a high temperature variation along the hot wall (~500°C). The temperature distribution along the wall was calculated from a 2D-axisymetrical finite volume simulation of our reactor using ANSYS-Fluent software. The model was calibrated by temperature measurement using both a bichromatic pyrometer on the graphite surface and a translating thermocouple along the axis of the reactor. Using both methods, simulated and experimental temperatures were in agreement within 30°C. Deposition was done on a graphite substrate as well as on a flexible graphite sheet covering the inner wall of the deposition chamber. In this study in particular, samples were collected all along the flexible graphite to probe different growth conditions, mainly temperature and gas composition. In the next parts, the samples will then be named after their position along the hot wall. Along the flexible graphite, circles of 20 mm diameter were collected to calculate an average growth rate by mass difference supposing the films were dense and fully covering the substrate. SEM cross-sectional images were also used to calculate growth rate.

2. Sample characterization

1. XRD

Θ-2θ (10-138°) scans in Bragg-Brentano geometry were performed using a powder diffractometer PANalytical X'Pert PRO MPD to characterize the preferential orientation of the samples at large scale (12*8 mm area). Variable divergence slit was used to keep a constant irradiated area at all angles. The Harris method [31] was used to characterize the texture of the sample. In this method, texture coefficients C_{hkl} are calculated as per reference from formula (1):

$$C_{khl} = (I_{hkl}/I_{0,hkl})/(1/N \cdot \sum \frac{I_{hkl}}{I_{0,hkl}}) \quad (1)$$

in which N is the number of peaks and I_{hkl} and $I_{0,hkl}$ are respectively the intensity of the (hkl) Bragg reflection for the sample studied and that of a randomly oriented sample, as given in file *00-029-1129* from the international center for diffraction data (ICDD) database. The effect of the variable divergence slit was accounted in the calculation of the relative intensities. The intensities were calculated from the area of the diffraction peaks. For the randomly oriented samples the value of all C_{hkl} is 1. For a perfectly oriented sample, the value of C_{hkl} is N. In the present case, 9 diffraction peaks were used, hence the highest possible C_{hkl} is 9, which would indicate a perfect preferential orientation along the corresponding <hkl> direction.

2. SEM & EBSD

Scanning electron microscopy (SEM) and electron back-scatter diffraction (EBSD) analysis were performed with a Zeiss Gemini S500 FEG equipped with a Velocity Super CMOS camera from EDAX. The sample preparation included standard diamond polishing down to 1 µm and a final colloidal silica (0.03 µm) polishing step. Vibratory polishing was carried out as a finishing step using colloidal silica (0.03 µm) for 2 hours. This step eliminates small scratches and surface damage, and leads to higher imaging quality in both BSE and EBSD modes.

The secondary electron mode was used to observe the morphology of the samples using an accelerating voltage of 5kV and a beam current of 0.2 nA. The back-scattered electron mode was used to reveal the crystallographic orientation contrast in cross-section at an accelerating voltage of 15 kV and a beam current of 3 nA.

EBSD maps were made with a 50 to 200 nm lateral step depending on the size of the map at an accelerating voltage of 20 kV and using a beam current of 11 nA. EBSD data treatments were performed with OIM data analysis software (EDAX). The data was cleaned using a grain dilatation method. Individual grains were defined as a group of 10 pixels with a tolerance angle of 5° between each pixel. Single average orientation was then computed for each individual grain. Grain boundaries (GB) were defined as a misorientation angle above 5° for two neighboring grains. Special types of grain boundary such as coincidence site lattice (CSL) Σ3, Σ9 and Σ27 GB were sought for according to the Brandon tolerance criteria [32]. Σ3 CSL are twin boundaries and stem from a 60° rotation around the <111> direction. The proportion of each GB was calculated in terms of length fraction, which is the ratio of the specific GB length over the total length of GBs.

III. Results and discussion

1. Growth rate along the hot wall

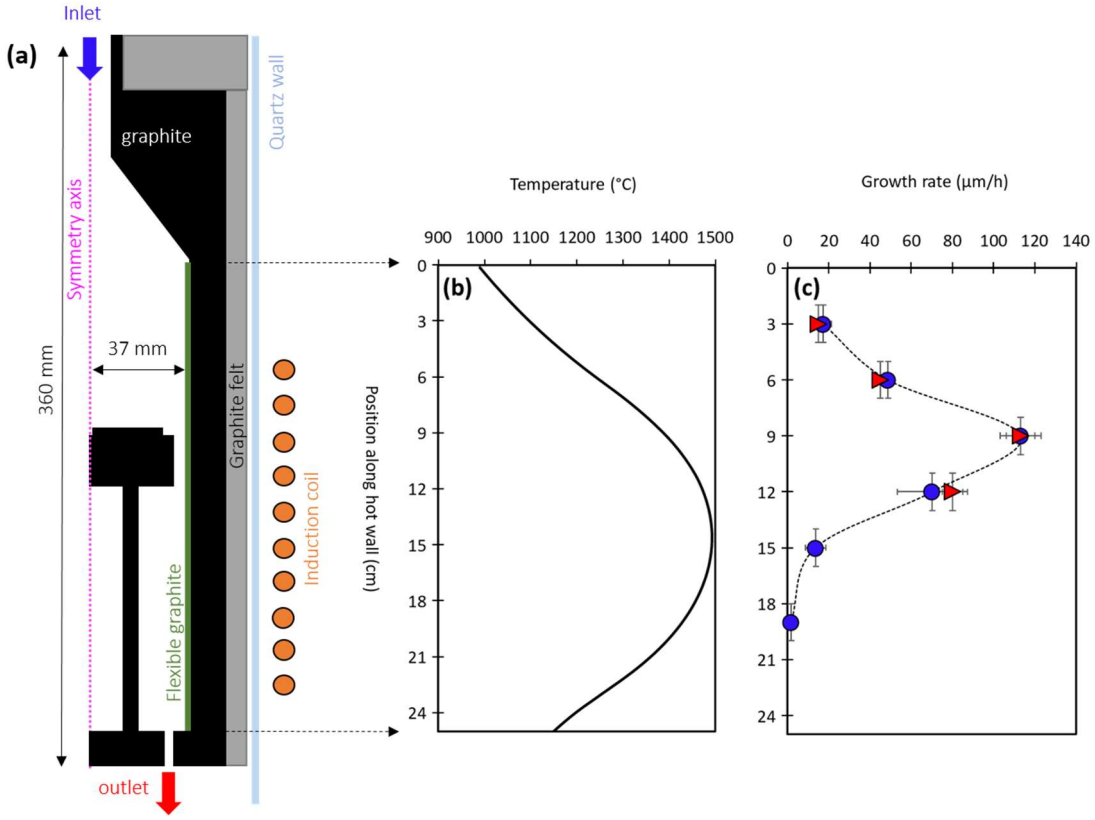

Figure 1: a) Scheme of the CVD reactor (axisymmetric representation). Samples were collected all along the hot wall on the flexible graphite b) Simulated temperature along the hot wall. c) Growth rate measured via weighing (●) and SEM cross sections (▲). Process parameters are: total flow rate = 1050 sccm; H_2:MTS = 10 ; total pressure = tens of mbar

Figure 1 shows the growth rate as well as the temperature profile along the hot wall. The growth rate first increases as temperature increases until 9 cm, where the temperature still increase but the growth rate starts to drop. This is due to reactant depletion after deposition on the wall upstream. Then, along the hot wall, each sample undergoes different growth conditions, in terms of both temperature and species partial pressure.

As microstructure development depends on these conditions, we decided to characterize the samples at positions 3, 6, 9, 12 and 15 cm along the hot wall.

2. Overview of the microstructure at large scale

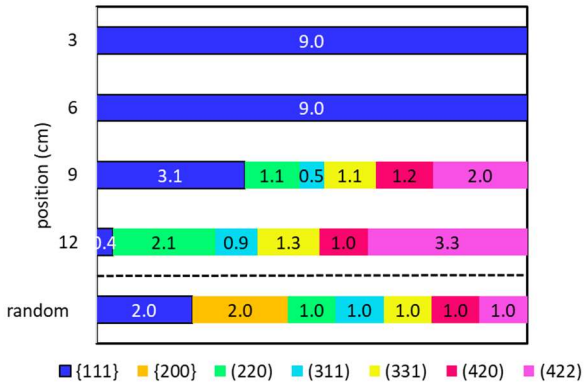

Figure 2: Texture coefficient (TC) chart for samples taken at positions 3, 6, 9 and 12 cm. TC were calculated over 9 {hkl} planes. $TC_{\{111\}}$ corresponds to the sum of (111) and (222) planes. $TC_{\{200\}}$ corresponds to the sum of (200) and (400) planes. TCs for a randomly oriented sample are given. If $TC_{hkl} > TC_{hkl,\ random}$ the corresponding plane is overrepresented, if $TC_{hkl} < TC_{hkl,\ random}$ it is underrepresented. A perfectly oriented sample would have a TC_{hkl} of 9, all other TC being zero.

Figure 2 shows the texture coefficients for the samples taken at different positions along the hot wall. Samples taken at 3 and 6 cm exhibit a strong <111> texture with a texture coefficient of 9. At 9 cm, a transition from <111> to a mix of <110> + <211> is observed. Other high angle planes are also present with texture coefficient close to unity. At 12 cm the texture is mainly <110> and <211> although other planes have a texture coefficient close to unity. Only the {111} and {200} families of planes are truly underrepresented, as indicated by a C_{hkl} of 0.4 for the former and 0 for the latter. Overall, the presence of multiple planes at 9 and 12 cm suggests a loss of preferential orientation. Plane (422) has been rarely reported in literature, likely due to the fact that XRD is often conducted on a narrower angular range, most of the time from $2\theta = 0°$ to 80°, neglecting the higher order planes. We discuss the occurrence of plane (422) in the following sections.

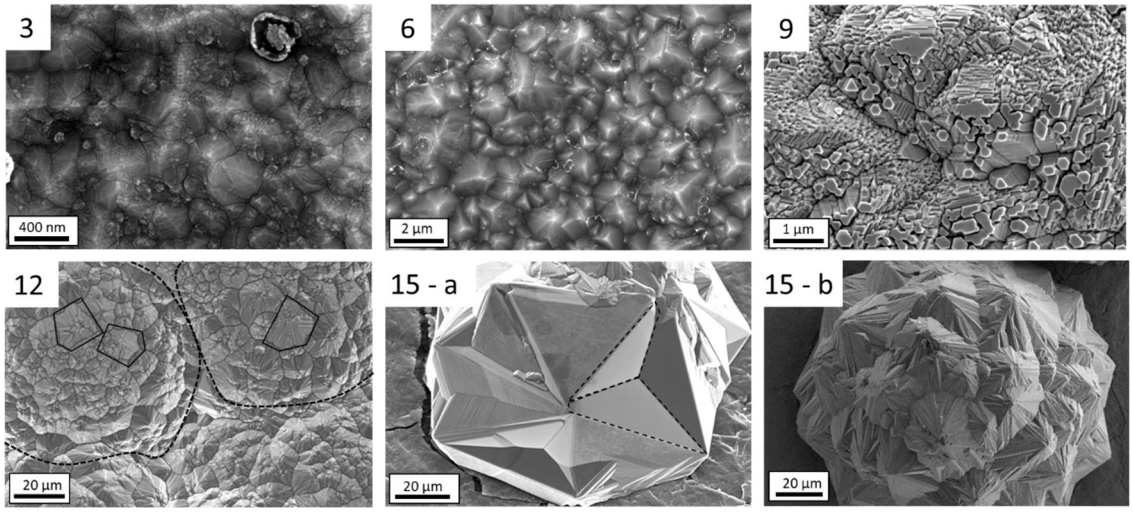

Figure 3: SEM-secondary electron surface morphology observation of samples taken at positions 3, 6, 9 , 12 , 15 cm.

Figure 3 shows the morphology of the deposit at different positions from 3 cm to 15 cm along the hot wall. For samples taken at 3 and 6 cm, faceted grains are observed with an irregular hexagonal morphology typical of twinned <111> oriented crystal. This is in accordance with the strong <111> texture observed by XRD for these two samples. For the sample taken at 9 cm, faceted grains can be seen with a well-defined hexagonal shape typical of twinned <111> oriented crystals. These grains are surrounded by a set of micro-facets. For the samples taken at 12 and 15 cm, large scale observation shows spherically shaped boules, which are compactly packed at 12 cm and individually separated at 15 cm. In both cases, pentagonal clusters of grains with many edges and grooves can be observed at a smaller scale.

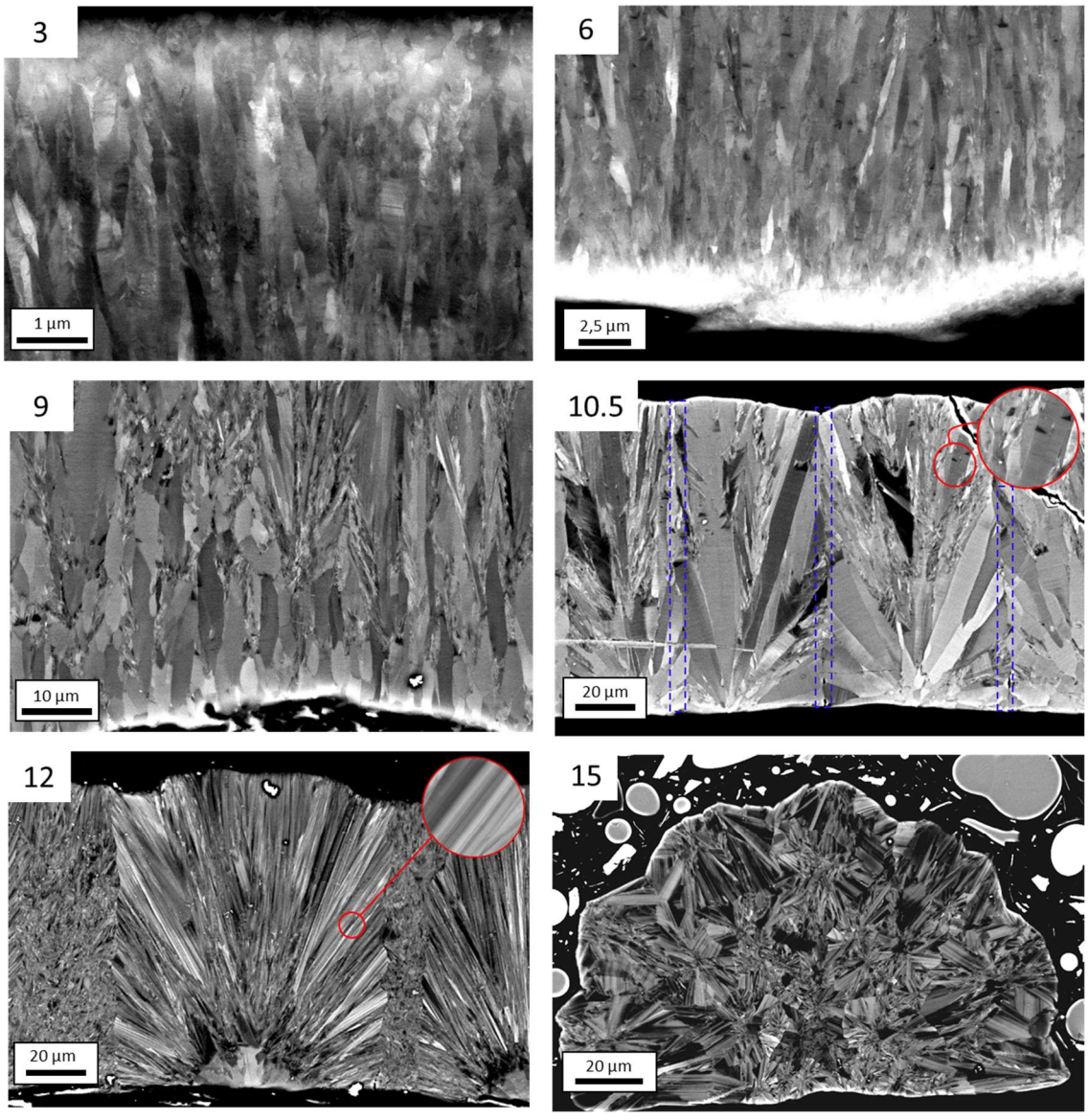

Figure 4: SEM-backscattered electron cross-sectional observation of samples taken at position 3, 6, 9, 10.5, 12, 15 cm

The samples from 3 to 9 cm are dense films, as confirmed by the corresponding cross sections shown in Figure 4. These cross-sections show long columnar grains with stripes perpendicular to the growth direction. These stripes are typical of micro-twins or successions of stacking faults on the {111} planes, as evidenced by high resolution

transmission electron microscopy (HR-TEM) in ref [10,11]. This indicates that the {111} planes are parallel to the sample surface which is also in accordance with the XRD results. The sample taken at 10.5 cm shows a “fireworks-like” growth with V-shaped grains whose length covers the entire layer thickness. The grains also exhibit stripes perpendicular to their fastest growth direction, indicating a preferential growth along the <111> direction, but the grains are now tilted compared to the substrate’s normal. This shows that growth took place in three dimensions, as spheres bonded to a substrate. However, the growth of multiple spheres next to each other hindered their lateral propagation as supported by the abrupt junction between groups of grains highlighted in blue in Figure 4. Overall, this indicates a lower nucleation frequency in favor of a grain growth regime. This is consistent with the higher temperature (1380°C) and hence the lower supersaturation [33–35]. The sample taken at 12 cm exhibits a similar 3D growth but the grains are now striped along their length. As mentioned before, these stripes are microtwins and stacking faults on the {111} planes, therefore indicating a change in preferential orientation of the grains with a fastest growth parallel to the {111} planes. Note also that the particular fireworks-like microstructure may explain the apparent decrease of preferential orientation observed by XRD for this sample. Indeed, while the grains have a preferential growth along a certain direction, a tilt of these grains with respect to the normal to the substrate surface reveals other crystallographic planes parallel to the sample surface. The cross-sectional observation of the sample taken at 15 cm shows the growth of large grains in three dimensions with several characteristic pentagonal structures pointing out of the micrographs. In this case, the growth of individual boules is observed and they are sufficiently far away from each other to allow 3D growth. Overall, the observed microstructure changes seem to be correlated to a change in growth regime and preferential orientation. This is mainly due to an increase of temperature and depletion of reactant along the hot wall of our CVD reactor. In order to obtain better insight into the underlying growth mechanism, further characterizations at grain scale are necessary.

3. Microstructure and orientations at grain scale

In order to fully characterize the microstructure at grain scale, EBSD was performed on samples taken at 12 and 15 cm. Figure 5 shows a low magnification view of multiple boules from the sample taken at 15 cm. From the inverse pole figure color code it can be seen that each center of the boules exhibits a <101> direction, equivalent to a <110> direction while the periphery is oriented towards <211>. Figure 6 shows IPF maps as well as maps of grain boundaries sorted by type. The pentagonal clusters can be clearly seen surrounded by high angle grain boundaries in which mainly twin boundaries are visible. Table 1 shows the statistical distribution of grain boundaries.

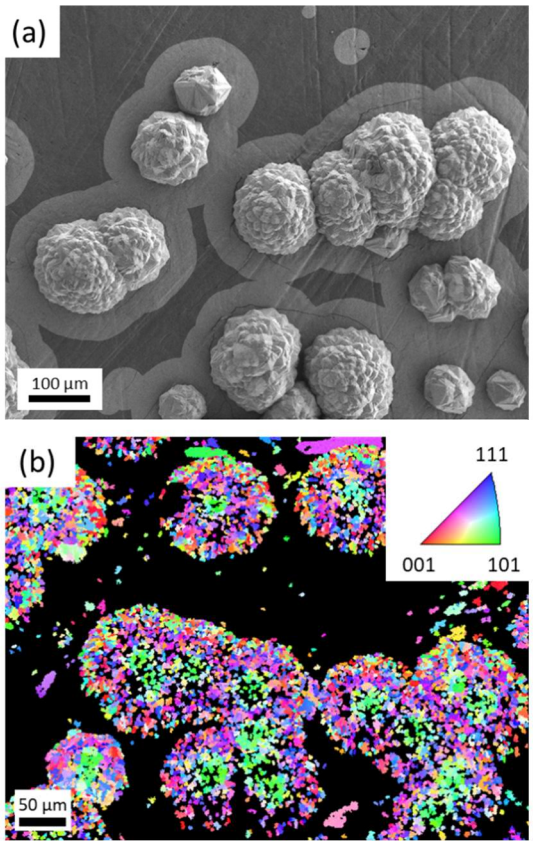

Figure 5: a) Surface morphology of the boules grown at a position of 15 cm along the wall, b) a top view EBSD inverse pole figure map of these boules. The boules were embedded in a resin and polished prior to observations.

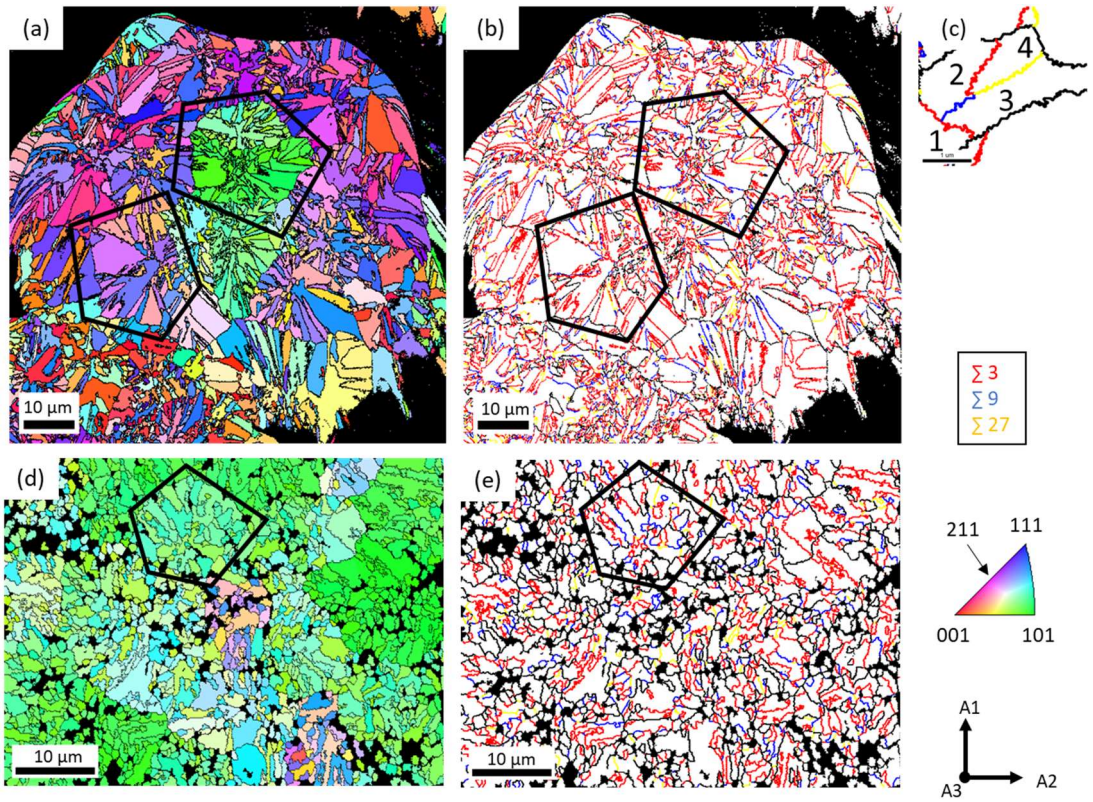

Figure 6: EBSD Inverse pole figure map for the sample taken at 15 cm (a) and at 12 cm (d) and the corresponding grain boundary maps (b), (e); (c) shows the CSL relationship in a cluster of 4 twinned grains. Orientations are given along axis A3 in the IPF maps.

Table 1: Statistics on grain boundaries (length fraction, in %) calculated from the corresponding EBSD maps in Figure 6.

Sample	GB (15-65°)	∑3	∑9	∑27
15 cm	18.7	63.7	11.0	6.7
12 cm	24.0	57.6	11.3	7.2

A very high fraction of Σ3 twin boundaries is observed, up to 60%. A significant fraction of Σ9 and Σ27 CSL GB (~15%) is also observed and can be interpreted as the interpenetration of twinned grains. This situation is depicted in Figure 6-(c). When two grains (2 & 3) are in twin relationship with a parent grain (1), the grain boundary they will form between each other is Σ3 x Σ3 = Σ9 GB. If another grain (4) is in twin relationship with one of the two primary twinned grains (2), the GB formed with grain (3) will be Σ9 x Σ3 = Σ27 GB. The twinning process in FCC grain growth can be attributed to a growth accident such as a stacking fault (SF) occurring on a {111} plane and propagating a twinned grain, for instance ABCA|B|ACBA if we consider a twinned stacking sequence of 3C-SiC along the <111> direction. Here, plane B located between the two A layers is the twin plane. SF energy is low in SiC (1.5 $mJ.m^{-2}$) [26], however, it cannot explain such a high fraction of twin boundaries. Therefore, this indicates that twinned grains are preferentially grown over non-twinned grains.

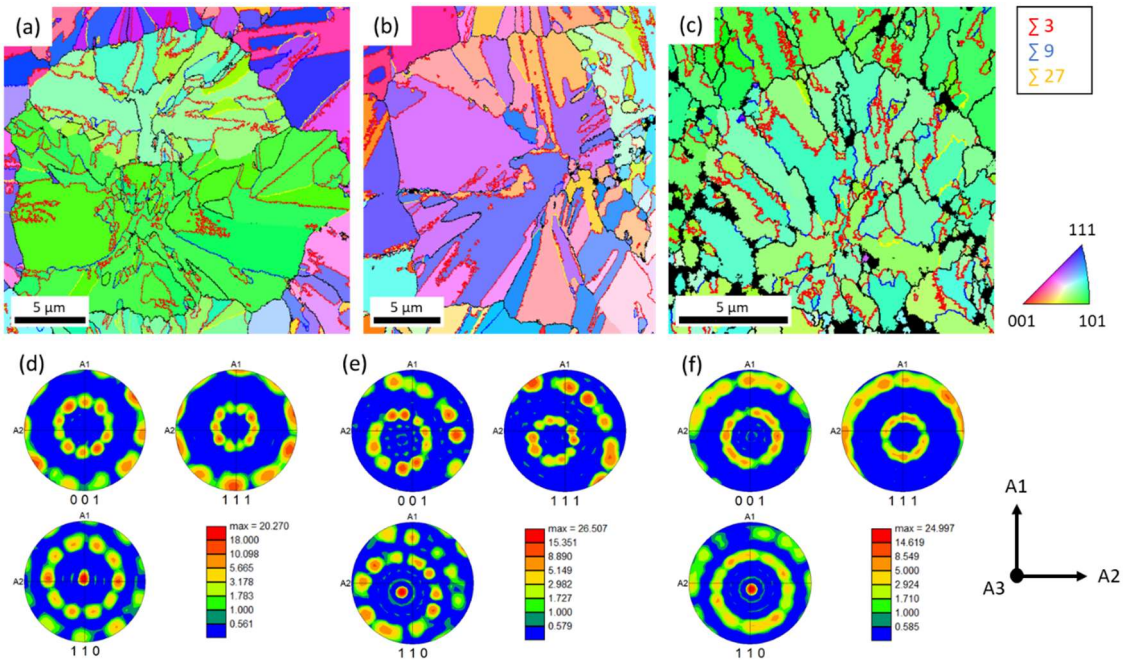

Figure 7: (a), (b), (c) Higher magnification view of the isolated pentagonal cluster highlighted in Figure 6. (d), (e), (f) The corresponding <001>, <111> and <110> pole figures. IPF maps and pole figures are given along axis A3.

A higher magnification view of individual 5-fold clusters is given in Figure 7. Pole figures are calculated from the orientation of each grain inside a single cluster. The <110> pole figure shows that every grain in the cluster shares a common <110> axis. The pole figure labeled (e) shows a deviation of the common <110> axis from the sample normal because the associated cluster is tilted with respect to the normal of the sample. Also visible are 10 discrete spots on the <001>, <110> and <111> pole figures that seem to be linked by a 10-fold symmetry axis. This reveals that a cluster is not simply fiber-textured but instead has a certain in-plane grain orientation. The origin of these particularities can be found in the growth scenario, which is discussed in the next section.

4. Discussion on the growth scenario

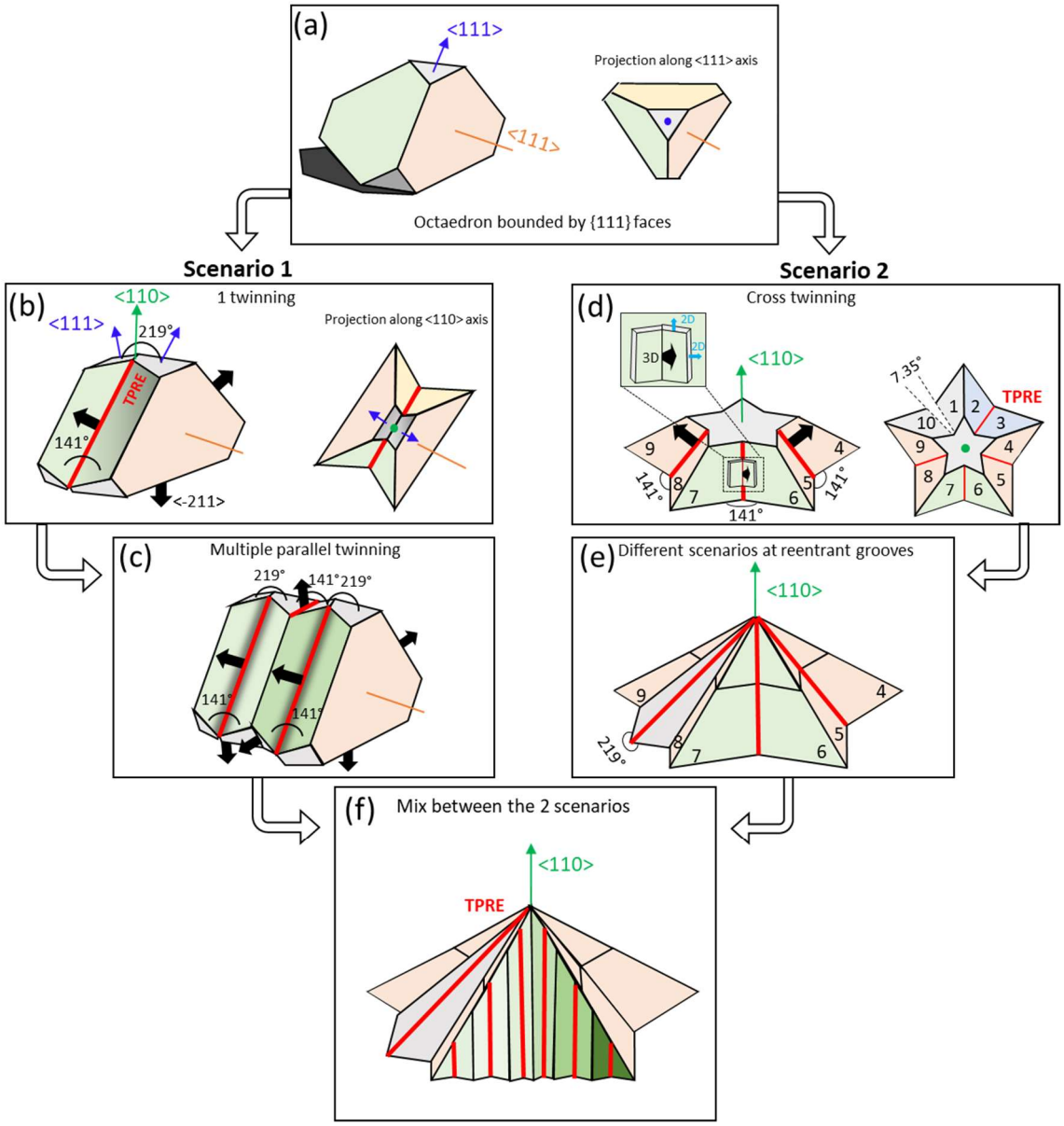

Figure 8: Different growth scenarios assisted by twinning events in a cubic crystal. (a) Side and top view of an octahedron bounded by {111} planes that is to be twinned along the <111> direction indicated in orange. (b) Side and top view of a singly twinned crystal derived from the initial octahedron. Red lines indicate twin plane reentrant edges (TPRE). Black arrows are the family of <211> growth directions. (c) Side view of a multiple parallel twinned crystal. (d) Side and top view of a cross-twinned crystal derived from the initial octahedron. The inset in the image shows a layer that nucleated at TPRE and that is growing laterally on the two twinned {111} planes. Further nucleation at TPRE leads to an outer growth. A 7.35° gap arises as a geometric consequence of the 4 successive cross-twins. (e) Side view of a cross-twinned crystal growing with different scenarios for each face. (f) Mix between the two scenarios: cross twinning with additional parallel twinning.

EBSD characterization revealed a very high fraction of twin boundaries inside the pentagonal clusters. All the grains in these clusters share a common [110] axis and are also oriented in the plane of the film, with what seems to be a 10-fold symmetry axis. In order to interpret this behavior, a scheme of the two elementary scenarios that can occur during the early-stage of growth and then promote further growth is represented in Figure 8. These scenarios are based on the Wagner-Hamilton-Seidensticker (WHS)

mechanism, often referred to as the twin plane re-entrant edge (TRPE) mechanism according to which, in a cubic system, atomic adsorption and nucleation occur preferentially on the reentrant grooves between two {111} planes formed by twinning. This favorable adsorption can be explained at the atomic scale by the fact that an adatom can find 4 nearest neighbors in the groove instead of 3 on a {111} plane, allowing the formation of more bonds which in turn lowers the nucleation barrier. The angle at the reentrant groove between 2 {111} planes is 141° and the direction pointing outwards from the groove is <211> [36]. Hence, after one twinning, three preferential <211> directions are formed, 120° apart. These directions are represented as black arrows in Figure 8-(b). After further growth, the groove becomes a ridge and at least one second twinning is necessary for this structure to achieve steady-state growth. Additional parallel twinning can occur and lead to multiple <211> preferential growth directions, as represented in Figure 8-(c). Note that in the case of parallel twinning, the <211> preferential growth directions are always contained in the twin plane, leading to preferential growth in two dimensions (scenario 1). The reader can refer to the original work for further details [37].

In 1996, Van de Waal [38] extended the WHS model and proposed a “cross twinning model” where a succession of twinning occur on planes non parallel to the first twin plane (scenario 2). If four non-parallel twin planes are formed, a star shaped morphology with a 7.35° gap will be observed with every twinned grain sharing a common [110] pseudo-five-fold axis. The situation is depicted in Figure 8-(d). As a result of the 7.35° gap, these structures must either contain defects in between the gap or be intrinsically strained. The four twin plane reentrant corners grow outwardly due to the preferential adsorption at this specific position, playing the role of a sink for surface species. The edges of the so initiated layer in between the protrusion arms are also a preferential site for incorporation and leads to 2D growth along the {111} planes as represented in the inset in Figure 8-(d). This lateral growth results in the upward growth of a tip at the center of the particle. The morphology of the 5-fold particle will depend on the relative nucleation rate (NR) at the reentrant groove and the lateral growth (LG) of the initiated layer. If NR > LG, many layers will emerge from the reentrant edge and even resemble to a tip at the macroscale. If NR ≈ LG or NR < LG, the reentrant corners will remain large at the macroscale with wide {111} terraces. These two situations are depicted in Figure 8-(e). Unlike the parallel twinned structure, the growth of the cross-twinned structure is 3D, with four <211> directions growing outwardly, and one <110> direction growing upwardly. Then, if we go back to the Van der Drift selection rule, a particle that has its <110> direction normal to the substrate surface will outgrow the neighboring grains, which will result in a strong <110> orientation, as depicted by the pole figures. Moreover, a tilt of the <110> direction with respect to the substrate’s normal will lead to a tilted growth accompanied by grain size enlargement owing to the fast lateral growth along the <211> directions. This is in good accordance with the cross-sectional observations. Additionally, as the cluster of grains exhibit four <211> directions of preferential growth, a 30° tilt with respect to the substrate’s normal will, statistically, lead to the occurrence of {211} planes parallel to the surface, which is in accordance with the XRD analysis and the SEM observations.

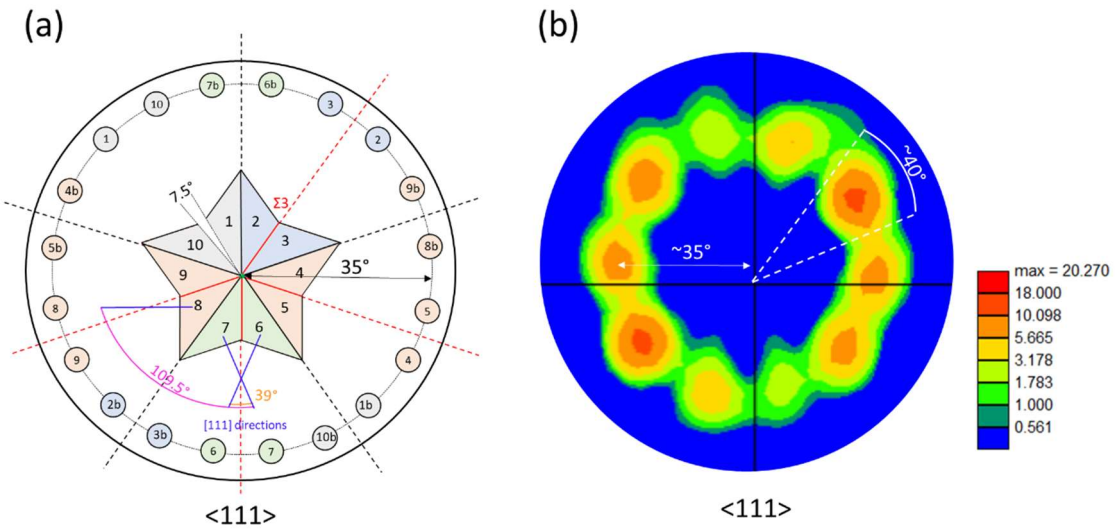

Figure 9: (a) Expected <111> pole figure for the cross-twinned pentagonal cluster. For the sake of clarity, the pole figure is represented on a 40° range. Blue lines stand for <111> directions. Red lines correspond to twin boundaries or equivalently TPRE. The two five-fold axes are represented in dashed red and black lines on the pole figure. (b) An experimental <111> pole figure of a pentagonal cluster, to be compared with the theoretical pole figure of a pentagonal cluster, as presented in (a).

Considering the geometry in Figure 8-(e), the theoretical projection on a pole figure is given in Figure 9-(a). A pseudo 5-fold symmetry axis would stand for each pair of <111> directions normal to the {111} plane separated by a twin boundary, namely for planes 2-3; 4-5 ; 6-7 ; 8-9 and 10-1. Each of these <111> directions would be separated by 180-141 = 39° on the stereographic representation. Another pseudo 5-fold symmetry axis would appear for each {111} plane that belongs to the same grain and that forms the branch of the star-like particle, namely planes 1-2; 3-4; 5-6; 7-8; 9-10. Geometrically, these planes are separated by 360-70.5 = 289.5°, therefore their normal are separated by 289.5-180 = 109.5°. Note that due to stereographical projection on both hemispheres, the intersection of the [111] direction from the corresponding plane labeled (1) in Figure 9 will intersect the northern hemisphere at position 1 and the southern hemisphere at position 1-b.The same applies to each [111] direction and leads to the appearance of a pseudo 10-fold symmetry axis for each pair of twinned {111} planes. By virtue of the symmetry of the cubic system, this pseudo ten-fold axis also applies to directions [001] and [110]. Finally, directions [111], [110] and [100] will appear 20 times on a pole figure. The experimental EBSD pole figure in Figure 9-(b) shows 10 spots, as large as 40°, separated by a pseudo-10-fold axis. The large spots are likely the unresolved pairs of {111} planes facing each other as well as their counterparts on the opposite hemisphere. This is supported by the relative intensities of the spots that are linked by a center of symmetry.

Therefore, the pole figures confirm the existence of multiple cross-twinned structure with a fivefold symmetry in <110> + <211> oriented samples. However, from the growth scenario presented in Figure 8-(e), we could expect a radial spreading of the grain boundaries from the center of the pentagonal cluster. When looking at these clusters in the EBSD maps, such behavior is generally not observed and they contain a much higher number of twinned grains, up to 50, whereas a perfect cross twinned structure would contain 5. What likely happened is a mix between the two growth scenarios, as presented in Figure 8-(f): a multiple cross-twinned structure with additional

twinning parallel to the first set of crossed twin planes. Indeed, when introducing additional twins parallel to the first set of crossed twins, they are not aligned anymore along the radius of the particle but they are rather parallel to it. This results in an increase of the number of twinned grains in the structure. The parallel twinning can also favor the interpenetration of successively twinned grains, hence the emergence of Σ9 and Σ27 GB, as observed in the EBSD maps. Additionally, the very high number of stripes, attributed to micro-twins, parallel to the growth direction as observed in the SEM cross sections further supports the hypothesis of parallel twinning. Note that the introduction of these parallel twin planes does not add any additional spots on the pole figure but can explain the bad resolution of the {111} pair facing each other due to the much higher number of twinned grains.

Overall, these observations support a growth mechanism assisted by multiple cross twinning and additional parallel twinning sequences. The origin of twinning in crystal growth is still under debate and there are two school of thoughts to address their formation: either the critical nucleus is originally twinned or it occurs during growth. Considering the second scenario, the emergence of Σ3 twins can be due to growth accidents, i.e. stacking faults on the {111} plane or alternatively as a way to relax growth stresses, also referred as to deformation twins [39]. For the former, the apparition of "accidental twinning" is then to be correlated with the stacking fault energy (SFE), i.e. the lower the SFEs, the easier the formation of twins. In literature, five-fold cross twinned structure have been observed in a number of materials grown by CVD such as diamond, Si, GaP, BN and TiN among others [39]. While SFE is low for SiC (1.5 $mJ.m^{-2}$ [26]), Si (30 $mJ.m^{-2}$ [40]) or GaP (41 $mJ.m^{-2}$ [41]) it is much higher for diamond (277 $mJ.m^{-2}$[26]), BN (184 $mJ.m^{-2}$ [26]) and TiN (1081 $mJ.m^{-2}$ [26]). Therefore, the growth of multiple cross twinned structure is not restricted to low SFE materials, suggesting that indeed their formation can be associated to other processes, either at the nucleation stage or during growth. Note that chemical impurities [39,42] or process conditions [43] might also play a role in favoring the emergence of twins, hence the formation of cross twinned structure. However, the very low SFE for SiC might explain the deviation from the perfect five-fold structure with additional parallel twinning sequences. More generally, twin mediated growth requires a low supersaturation regime to prevent 2D nucleation on the {111} faces and promote adatom migration towards the preferential site of incorporation, i.e. the TPREs. In CVD, supersaturation increases when the temperature decreases and the species partial pressure increases [33–35]. In our experiment, the transition from a <111> to a <110> texture is observed when the temperature is increased above 1380 °C. Additionally, the amount of reactive species must decrease as the gas progresses along the hot wall due to deposition. This also agrees with the occurrence of the <110> texture downstream of the gas flow, from 12 cm. To get a better picture of the evolution of species partial pressure along the deposition zone, CFD simulation including temperature distribution, flow and kinetics would be of great interest. This will be the topic of a forthcoming paper.

IV. Conclusion

Using a hot wall CVD reactor with a well-described temperature profile along the hot wall allowed us to probe the effect of the local growth conditions on the crystallographic orientations of polycrystalline 3C-SiC deposits in a single experiment.

Highly oriented <111> films were obtained at low temperature and high precursor partial pressure. The progressive transition to a mix of <110> and <211> preferential orientation was observed when the temperature increased, typically up to 1380°C, and the reactive species concentration decreased due to their consumption along the hot wall. These orientations were attributed to a twin mediated growth mechanism, supported by thorough EBSD characterization. The activation of such a mechanism is associated with the decrease of supersaturation and the increase of temperature, which essentially lowers the nucleation frequency and enhances the surface mobility of adatoms. This promotes diffusion of adsorbed species to the twin plane reentrant grooves that act as preferential sites for incorporation and that favors the growth along the <211> direction. If cross-twinning occurs, cluster of twinned grain sharing a common <110> axis can be formed, arranging according to a pseudo five-fold symmetry axis. In most samples, we observed a deviation from a perfect cross-twinned structure with additional twin planes parallel to the first set of crossed twins leading to clusters of up to 50 twinned grains, yet still arranged according to a pseudo fivefold axis. These multiply twinned clusters grow faster in three dimensions which results in a strong <110> orientation of the film, according to the Van der Drift selection rule.

V. Acknowledgements

The authors thanks MERSEN for the financial support. Florence Robaut is gratefully acknowledged for her technical support in the EBSD characterization. Stephane Coindeau and Thierry Encinas are gratefully acknowledged for the XRD characterization. Roman Reboud is gratefully acknowledged for the help in the conception and maintenance of the CVD reactor.

VI. References

[1] C.A. Zorman, M. Mehregany, Silicon carbide for MEMS and NEMS - an overview, in: Proceedings of IEEE Sensors, IEEE, Orlando, FL, USA, 2002: pp. 1109–1114. https://doi.org/10.1109/ICSENS.2002.1037269.

[2] R.G. Azevedo, D.G. Jones, A.V. Jog, B. Jamshidi, D.R. Myers, L. Chen, X. Fu, M. Mehregany, M.B.J. Wijesundara, A.P. Pisano, A SiC MEMS Resonant Strain Sensor for Harsh Environment Applications, IEEE Sensors J. 7 (2007) 568–576. https://doi.org/10.1109/JSEN.2007.891997.

[3] J. Chin, P.K. Gantzel, R.G. Hudson, The structure of chemical vapor deposited silicon carbide, Thin Solid Films. 40 (1977) 57–72. https://doi.org/10.1016/0040-6090(77)90103-1.

[4] M.G. So, J.S. Chun, Growth and structure of chemical vapor deposited silicon carbide from methyltrichlorosilane and hydrogen in the temperature range of 1100 to 1400°C, Journal of Vacuum Science and Technology A: Vacuum, Surfaces and Films. 6 (1988) 5–8. https://doi.org/10.1116/1.574969.

[5] D.J. Cheng, W.J. Shyy, D.H. Kuo, M.H. Hon, Growth Characteristics of CVD Beta-Silicon Carbide, J. Electrochem. Soc. 134 (1987) 3145–3149. https://doi.org/10.1149/1.2100359.

[6] D.-J. Kim, D.-J. Choi, Y.-W. Kim, Effect of reactant depletion on the microstructure and preferred orientation of polycrystalline SiC films by chemical vapor deposition, Thin Solid Films. 266 (1995) 192–197. https://doi.org/10.1016/0040-6090(96)80023-X.

[7] Y. Kajikawa, S. Noda, H. Komiyama, Preferred Orientation of Chemical Vapor Deposited Polycrystalline Silicon Carbide Films, Chemical Vapor Deposition. 8 (2002) 99–104. https://doi.org/10.1002/1521-3862(20020503)8:3<99::Aid-cvde99>3.0.Co;2-c.

[8] V. Radmilovic, U. Dahmen, D. Gao, C.R. Stoldt, C. Carraro, R. Maboudian, Formation of fiber texture in β-SiC films deposited on Si(100) substrates, Diamond and Related Materials. 16 (2007) 74–80. https://doi.org/10.1016/j.diamond.2006.03.017.

[9] R. Tu, D. Zheng, Q. Sun, M. Han, S. Zhang, Z. Hu, T. Goto, L. Zhang, Ultra-Fast Fabrication of -Oriented β-SiC Wafers by Halide CVD, J. Am. Ceram. Soc. 99 (2016) 84–88. https://doi.org/10.1111/jace.13980.

[10] Z. Hu, D. Zheng, R. Tu, M. Yang, Q. Li, M. Han, S. Zhang, L. Zhang, T. Goto, Structural Controlling of Highly-Oriented Polycrystal 3C-SiC Bulks via Halide CVD, Materials. 12 (2019) 390. https://doi.org/10.3390/ma12030390.

[11] Y. Lai, S. Zhao, T. Luo, Q. Xu, C. Liu, K. Liu, Q. Li, M. Yang, S. Zhang, M. Han, T. Goto, R. Tu, Microstructure and texture of polycrystalline 3C–SiC thick films characterized via EBSD, Ceramics International. 46 (2020) 27000–27009. https://doi.org/10.1016/j.ceramint.2020.07.177.

[12] J.-J. Huang, C. Militzer, C. Wijayawardhana, U. Forsberg, L. Ojamäe, H. Pedersen, Controlled CVD Growth of Highly ⟨111⟩-Oriented 3C-SiC, J. Phys. Chem. C. (2022) 8. https://doi.org/10.1021/acs.jpcc.2c01171.

[13] Y. Long, A. Javed, Z. Chen, X. Xiong, P. Xiao, Deposition Rate, Texture, and Mechanical Properties of SiC Coatings Produced by Chemical Vapor Deposition at Different Temperatures, Int. J. Appl. Ceram. Technol. 10 (2013) 11–19. https://doi.org/10.1111/j.1744-7402.2012.02786.x.

[14] H. Cheng, M. Yang, Y. Lai, M. Hu, Q. Li, R. Tu, S. Zhang, M. Han, T. Goto, L. Zhang, Transparent highly oriented 3C-SiC bulks by halide laser CVD, Journal of the European Ceramic Society. 38 (2018) 3057–3063. https://doi.org/10.1016/j.jeurceramsoc.2018.03.015.

[15] Y. Long, A. Javed, I. Shapiro, Z. Chen, X. Xiong, P. Xiao, The effect of substrate position on the microstructure and mechanical properties of SiC coatings on carbon/carbon composites, Surface and Coatings Technology. 206 (2011) 568–574. https://doi.org/10.1016/j.surfcoat.2011.07.087.

[16] T. Dn, W. L, T. Cc, F. Zc, Assessing Biaxial Stress and Strain in 3C-SiC/Si (001) by Raman Scattering Spectroscopy, J Material Sci Eng. 06 (2017). https://doi.org/10.4172/2169-0022.1000324.

[17] Van der Drift, Evolutionary selection, a principle governing growth orientation in vapour deposited layers, Philips Res. Rep. 22 (1967) 267–288.

[18] D.N. Lee, texture and structure of vapor deposit, Journal of Materials Science. 34 (1999) 2575–2582. https://doi.org/10.1023/A:1004696531491.

[19] J.-M. Zhang, F. Ma, K.-W. Xu, Calculation of the surface energy of FCC metals with modified embedded-atom method, Applied Surface Science. 229 (2004) 34–42. https://doi.org/10.1016/j.apsusc.2003.09.050.

[20] Lee, Dong Nyung, A model for development of orientation of vapour deposits, Journal of Materials Science. 24 (1989) 4375–4378. https://doi.org/ttps://doi.org/10.1007/BF00544515.

[21] S. Liu, X. Luo, B. Huang, Y. Yang, Influence of Supersaturation on Growth Behavior and Mechanical Properties of Polycrystalline 3C-SiC on W Wire Substrate, (2022) 18.

[22] H. Cheng, R. Tu, S. Zhang, M. Han, T. Goto, L. Zhang, Preparation of highly oriented β-SiC bulks by halide laser chemical vapor deposition, Journal of the European Ceramic Society. 37 (2017) 509–515. https://doi.org/10.1016/j.jeurceramsoc.2016.09.017.

[23] Ö. Danielsson, H. Pedersen, L. Ojamäe, Perspective—Current Understanding of the Halogenated Deposition Chemistry for Chemical Vapor Deposition of SiC, ECS J. Solid State Sci. Technol. 9 (2020) 104006. https://doi.org/10.1149/2162-8777/abbf2e.

[24] P. Sukkaew, Ö. Danielsson, O. Kordina, E. Janzén, L. Ojamäe, Ab Initio Study of Growth Mechanism of 4H–SiC: Adsorption and Surface Reaction of C_2H_2, C_2H_4, CH_4, and CH_3, J. Phys. Chem. C. 121 (2017) 1249–1256. https://doi.org/10.1021/acs.jpcc.6b11085.

[25] Ö. Danielsson, P. Sukkaew, E. Kalered, E. Janzén, O. Kordina, L. Ojamäe, Growth Mechanism of SiC Chemical Vapor Deposition: Adsorption and Surface Reactions of Active Si Species, J. Phys. Chem. C. 122 (2018) 648–661. https://doi.org/10.1021/acs.jpcc.7b10751.

[26] Y. Zhang, Z.-R. Liu, D.-W. Yuan, Q. Shao, J.-H. Chen, C.-L. Wu, Z.-L. Zhang, Elastic Properties and Stacking Fault Energies of Borides, Carbides and Nitrides from First-Principles Calculations, Acta Metall. Sin. (Engl. Lett.). 32 (2019) 1099–1110. https://doi.org/10.1007/s40195-019-00873-8.

[27] Min-Hsiung Hon, Yung-Ming Lu, Chun-Hsun Chu, Growth characteristics of B-SiC by chemical vapour deposition, Journal of Materials Science. 27 (1992) 3883–3888. https://doi.org/10.1007/BF00545472.

[28] H. Cheng, T.-T. Lin, M.-H. Hon, Multiple twind induced <110> preferred growth in TiN and SiC films prepared by CVD, Scripta Materialia. 35 (1996) 113–116. https://doi.org/10.1016/1359-6462(96)00091-7.

[29] M.X. Han, W. Zhou, D.H. Zheng, R. Tu, S. Zhang, T. Goto, Effects of C/Si Ratio on the Structure of β-SiC Film by Halide CVD, KEM. 616 (2014) 227–231. https://doi.org/10.4028/www.scientific.net/KEM.616.227.

[30] H. Plaisantin, J. Danet, I. Berdoyes, G. Laduye, A. Desenfant, G. Chollon, Structure, microstructure and disorder in low temperature chemical vapor deposited SiC coatings, Journal of the European Ceramic Society. 43 (2023) 3917–3930. https://doi.org/10.1016/j.jeurceramsoc.2023.02.067.

[31] G.B. Harris, X. Quantitative measurement of preferred orientation in rolled uranium bars, The London, Edinburgh, and Dublin Philosophical Magazine and Journal of Science. 43 (1952) 113–123. https://doi.org/10.1080/14786440108520972.

[32] D.G. Brandon, The structure of high-angle grain boundaries, Acta Metallurgica. 14 (1966) 1479–1484. https://doi.org/10.1016/0001-6160(66)90168-4.

[33] G. Chichignoud, M. Ucar-Morais, M. Pons, E. Blanquet, Chlorinated silicon carbide CVD revisited for polycrystalline bulk growth, Surface and Coatings Technology. 201 (2007) 8888–8892. https://doi.org/10.1016/j.surfcoat.2007.04.113.

[34] D. Lespiaux, F. Langlais, R. Naslain, S. Schamm, J. Sevely, Correlations between gas phase supersaturation, nucleation process and physico-chemical characteristics of silicon carbide deposited from Si-C-H-Cl system on silica substrates, Journal of Materials Science. 30 (1995) 1500–1510. https://doi.org/10.1007/BF00375255.

[35] J.-O. Carlsson, The relationship between deposition rate and supersaturation in the chemical vapor deposition of boron, Journal of the Less-Common Metals. 70 (n.d.) 97–106. https://doi.org/10.1016/0022-5088(80)90276-3.

[36] A.J. Shahani, E.B. Gulsoy, S.O. Poulsen, X. Xiao, P.W. Voorhees, Twin-mediated crystal growth: an enigma resolved, Sci Rep. 6 (2016) 28651. https://doi.org/10.1038/srep28651.

[37] D.R. Hamilton, R.G. Seidensticker, Propagation Mechanism of Germanium Dendrites, Journal of Applied Physics. 31 (1960) 1165–1168. https://doi.org/10.1063/1.1735796.

[38] B.W. van de Waal, Cross-twinning model of fcc crystal growth, Journal of Crystal Growth. 158 (1996) 153–165. https://doi.org/10.1016/0022-0248(95)00419-X.

[39] H. Hofmeister, Fivefold twinned nanoparticles, Encyclopedia of Nanoscience and Nanotechnology. 3 (2004) 431–452.

[40] M.Y. Chou, M.L. Cohen, S.G. Louie, Theoretical study of stacking faults in silicon, Phys. Rev. B. 32 (1985) 7979–7987. https://doi.org/10.1103/PhysRevB.32.7979.

[41] S. Takeuchi, K. Suzuki, K. Maeda, H. Iwanaga, Stacking-fault energy of II–VI compounds, Philosophical Magazine A. 50 (1985) 171–178. https://doi.org/10.1080/01418618408244220.

[42] A.J. Shahani, P.W. Voorhees, Twin-mediated crystal growth, J. Mater. Res. 31 (2016) 2936–2947. https://doi.org/10.1557/jmr.2016.308.

[43] T. Liu, D. Raabe, W. Mao, S. Zaefferer, Microtexture and Grain Boundaries in Freestanding CVD Diamond Films: Growth and Twinning Mechanisms, Adv. Funct. Mater. 19 (2009) 3880–3891. https://doi.org/10.1002/adfm.200901231.